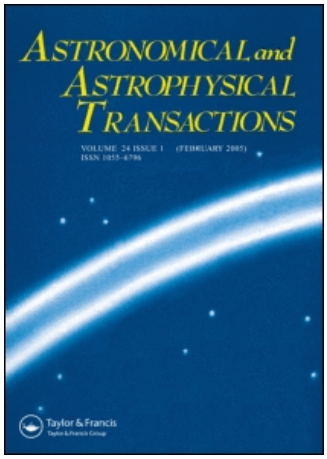

Astronomical & Astrophysical Transactions
The Journal of the Eurasian Astronomical Society
Publication details, including instructions for authors and subscription information:
http://www.informaworld.com/smpp/title~content=t713453505

Leo II Group: decoupled cores of NGC 3607 and NGC3608

V. L. Afanasiev [a]; O. K. Silchenko [bc]
[a] Special Astrophysical Observatory, Nizhnij Arkhyz, Russia
[b] Sternberg Astronomical Institute, Moscow, Russia
[c] UK Astronomy Data Centre, Guest Investigator,

Online Publication Date: 01 August 2007
To cite this Article: Afanasiev, V. L. and Silchenko, O. K. (2007) 'Leo II Group: decoupled cores of NGC 3607 and NGC3608', Astronomical & Astrophysical Transactions, 26:4, 311 - 337
To link to this article: DOI: 10.1080/10556790701553524
URL: http://dx.doi.org/10.1080/10556790701553524

Astronomical and Astrophysical Transactions
Vol. 26, Nos. 4–5, August–October 2007, 311–337

Leo II Group: decoupled cores of NGC 3607 and NGC3608

V. L. AFANASIEV*† and O. K. SILCHENKO‡§

†Special Astrophysical Observatory, Nizhnij Arkhyz, 369167, Russia
‡Sternberg Astronomical Institute, University av. 13, Moscow 119991, Russia
§UK Astronomy Data Centre, Guest Investigator

(Received 20 June 2007)

The kinematics, structure, and stellar population properties in the centres of two brightest early-type galaxies of the Leo II group, NGC 3607 and NGC 3608, are studied by means of integral-field spectroscopy. The kinematically distinct areas in the centres of these galaxies, with radii of 6″ and 5″, respectively, are found also to be chemically distinct: they are characterized by enhanced magnesium-line strength. However, no stellar age differences have been found between the decoupled cores and their outskirts. An analysis of two-dimensional line-of-sight velocity fields reveals systematic turns of kinematical major axes near the nuclei of both galaxies; in NGC 3608 the ionized gas rotates perpendicular to the stellar component rotation. When taking into account some morphological features, it is concluded that both NGC 3607 and NGC 3608 have large triaxial stellar spheroids. it is argued that the magnesium-enhanced cores are not circumnuclear disks; instead they resemble rather compact triaxial structures that force the formation of polar disks around them – a gaseous one in NGC 3608 and a stellar-gaseous one in NGC 3607; in the latter, star formation is perhaps still proceeding.

Keywords: Galaxies: individual: NGC 3607 – Galaxies: individual: NGC 3608 – Galaxies: nuclei – Galaxies: stellar content – Galaxies: kinematics & dynamics – Galaxies: evolution

1. Introduction

There exist now certain contradictions between a homogeneous red-colour appearance of nearby early-type galaxies, implying a rather brief ancient epoch of the main star formation, and prescriptions of the hierarchical concept of galaxy formation requiring quite recent merger events followed by some secondary (nuclear) star formation. Galaxy groups represent perhaps the best places where signatures of the external-driven secular evolution in early-type galaxies may be found because dense environments and moderate (with respect to clusters') velocity dispersions are favourable for mergers and tidal interactions.

Recently we have considered Leo I group and its members NGC 3379, NGC 3384, and NGC 3368 [1]. A combined analysis of the stellar and gaseous kinematics and of stellar population properties in the centres of galaxies has revealed signatures of synchronous secular

*Corresponding author. Email: vafan@sao.ru

Astronomical and Astrophysical Transactions
ISSN 1055-6796 print/ISSN 1476-3540 online © 2007 Taylor & Francis
http://www.tandf.co.uk/journals
DOI: 10.1080/10556790701553524

evolution: inner rotation axes are aligned, despite the different orientations of the outer galactic bodies, and the mean stellar age estimates are evidence for quasi-simultaneous star formation bursts about 3 Gyr ago. However, the Leo I group is unique in some sense because it possesses a supergiant intergalactic H I cloud of $1.7 \cdot 10^9\, M_\odot$ [2], [3]; its shape is a clumpy ring with a radius of $\sim$100 kpc encircling the galaxy pair NGC 3379/NGC 3384, and just the spatial orientation of this ring defines the alignment of the inner rotation axes of the three galaxies. So it seems probable that the secular evolution of the Leo I early-type galaxies is governed by the tidal interaction of every galaxy with the intergalactic H I ring and not by the tidal interactions between the galaxies. Now we are going to study central early-type galaxies of the Leo II group lacking considerable masses of neutral hydrogen. It is interesting to look for signatures of the secular evolution in the circumnuclear parts of these galaxies. The Leo II group contains 16 galaxies brighter than $B_T \approx 16$, according to [4]. Of those, only five are of early type, namely, S0 or ellipticals; and three early-type galaxies, NGC 3605 (compact dwarf elliptical), NGC 3607, and NGC 3608 are located in the very centre of the group within a 60 kpc area. The velocity dispersion of the whole group is rather moderate, 417 km/s according to [5].

The main characteristics of the galaxies to be considered in the present paper are given in table 1. NGC 3607 is a giant lenticular galaxy located in the centre of the Leo II group. Hot X-ray gas is detected inside this galaxy [6], as well as around it [7] – obviously, all the central galaxies of the group are embedded into a common envelope of hot gas. A new X-ray map of the group in the atlas [9] demonstrates two maxima of the hot gas concentration – one at NGC 3607 and another at NGC 3608 – which forces authors to state a recent merger history of the Leo II group. Also NGC 3607, though of early type, is known to have a rather extended central ionized-gas disk ([10], [11]) with a radius of $\sim 15''$ ($\sim$1.5 kpc) containing a broad dust ring between $R = 8.4''$ and $R = 13.2''$ [12]. A central structure of the neighbouring low-luminosity elliptical galaxy NGC 3608 is also very interesting: it has a counterrotating core. Basing on a long-slit cross-section taken along the major axis of NGC 3608 it is noted by [13] that at approximately $R = 10''$ (1.1 kpc) the stellar rotation changes its sense; the maximum rotation velocity of the inner core, achieved at $R \approx 4''$, was, however, rather low, of $\sim$15 km/s. In [14] high-resolution images are inspected that have been obtained with the WFPC2/HST through two filters, F555W and F814W, for the sample of elliptical galaxies with kinematically decoupled cores, and particularly in NGC 3608 no evidence has been found for

Table 1. Global parameters of the galaxies.

NGC	3607	3608
Type (NED[1])	SA(s)0*	E2
R_{25}, kpc (LEDA[2])	15.2	10.5
B_T^0 (RC3[3])	10.79	11.69
M_B(LEDA)	−20.00	−19.74
$(B-V)_T^0$ (RC3)	0.92	0.93
$(U-B)_T^0$(RC3)	0.49	0.40
V_r(NED), km·s^{-1}	935	1253
Distance, Mpc	23[4]	
Inclination (LEDA)	34°	52°
PA_{phot} (LEDA)	120°	80°
σ_*, km·s^{-1}(LEDA)	224	192

[1]NASA/IPAC Extragalactic Database.
[2]Lyon-Meudon Extragalactic Database.
[3]Third Reference Catalogue of Bright Galaxies.
[4][8].

a circumnuclear stellar disk presence. In this work it was claimed that the colour $V - I$ is very homogeneous over the central parts of the sample galaxies, the kinematically decoupled cores being indistinctive from the surrounding stellar bodies; in the particular case of NGC 3608, however, we suspect a break of $V - I$ by less than 0.1 mag at $R \approx 4''$ from their figure 1d. Curiously, though neither [14] nor other investigators find any fine morphological substructure in NGC 3608, the global properties of the galaxy look unusual: despite its low luminosity, it is a slow rotator [13], it is boxy [15], and it has a shallow core profile [14] – a classic set of properties of a giant elliptical. A general view of both galaxies is presented by figures 1 and 2 where three various fields of view are outlined: the large-scale view of the galaxies, the HST/PC-frame field, and the central regions observed by means of 2D spectroscopy.

The layout of the paper is as follows. We report our observations and other data which we use in section 2. The radial variations of the stellar population properties are analysed in section 3, and in section 4 2D velocity fields obtained by means of 2D spectroscopy for the central parts of NGC 3607 and NGC 3608 are presented. Section 5 provides a discussion and our conclusions.

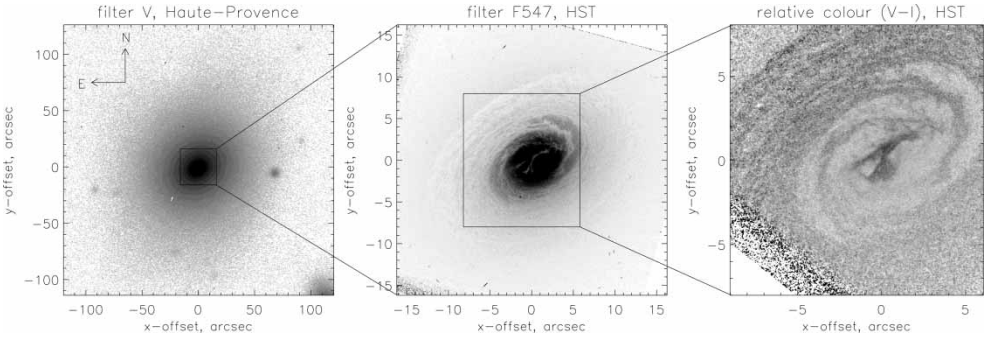

Figure 1. The photometric maps for NGC 3607: *left* – large-scale image through the filter V (Haute-Provence data from the HYPERLEDA database), intensity is linearly gray-scaled, *middle* – the HST/PC frame through the filter F547M, the same, *right* – the area observed with the Multi-Pupil Fiber Spectrograph, with the uncalibrated colour distribution obtained by dividing the HST/PC frames through the filters F814W and F555W by each other and taking 2.5 logarithms, darker means redder.

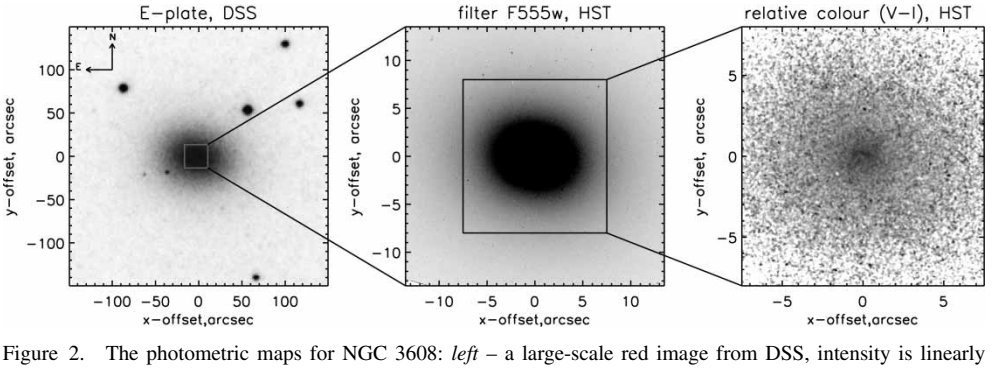

Figure 2. The photometric maps for NGC 3608: *left* – a large-scale red image from DSS, intensity is linearly gray-scaled, *middle* – the HST/PC frame through the filter F555W, the same, *right* – the area observed with the Multi-Pupil Fiber Spectrograph, with the uncalibrated colour distribution obtained by dividing the HST/PC frames through the filters F814W and F555W by each other and taking 2.5 logarithms, darker means redder.

2. Observations and data reduction

The spectral data analysed in this work are obtained using two different integral-field spectrographs. Integral-field spectroscopy is a rather new approach which was first proposed by Professor G. Courtes some 25 years ago – for a description of the idea behind the instrument see [16]. It allows one to obtain simultaneously a set of spectra over a wide spectral range from an extended area of the sky, for example, from the central part of a galaxy. In the spectrographs which we use, a 2D array of microlenses provides a set of micropupils which are put onto the spectrograph, so after having reduced the full set of spectra corresponding to the individual spatial elements, we obtain a list of fluxes in continuum and in emission lines, of line-of-sight velocities, both for stars and ionized gas, and of absorption-line equivalent widths, which are usually expressed as indices in the well-formulated Lick system [17]. This list can be transformed into 2D maps of the above mentioned characteristics for the central part of a galaxy. Besides the panoramic view benefits, such an approach gives a unique opportunity to overlay various 2D distributions over each other without any difficulties with positioning. In this work we use data from two 2D spectrographs: the fibre-lens Multi-pupil Fiber Spectrograph (MPFS) at the 6 m telescope of the Special Astrophysical Observatory of the Russian Academy of Sciences (SAO RAS) and the international Tiger-mode SAURON at the 4.2 m William Herschel Telescope at La Palma. SAURON is a private spectrograph, but its data are available after expiration to everybody, from the Isaac Newton Group Archive in the UK Astronomy Data centre.

The last variant of the MPFS became operational in the prime focus of the 6 m telescope in 1998: (http://www.sao.ru/hq/lsfvo/devices/mpfs/mpfs_main.html) [18].

With respect to the previous variant, in the new MPFS the field of view is increased and the common spectral range is larger due to the use of fibres: they transmit light from 16×15 square elements of the galaxy image to the slit of the spectrograph together with an additional 16 fibres that transmit the sky background light taken a few arcminutes apart from the galaxy, so that separate sky exposures are not necessary now. The size of one spatial element was approximately $1'' \times 1''$; a CCD TK 1024×1024 detector was used before 2003. The reciprocal dispersion is 1.35 Å per pixel, with a spectral resolution of 5 Å rather stable over the field of view. To calibrate the wavelength scale, we expose separately a spectrum of the hollow cathode lamp filled with helium, neon, and argon; an internal accuracy of linearization was typically 0.25 Å in the green and 0.1 Å in the red, and additionally we checked the accuracy and for the absence of systematic velocity shift by measuring strong emission lines of the night sky [OI]λ5577 and [OI]λ6300. We obtain MPFS data in two spectral ranges, the green one, 4300–5600 Å, and the red one, 5900–7200 Å.

The green spectra are used to calculate the Lick indices Hβ, Mgb, Fe5270, and Fe5335, which are suitable to determine metallicity, age, and Mg/Fe ratio of old stellar populations [19]. To calibrate the new MPFS index system onto the standard Lick system, we have observed 15 stars from the list of [17] during four observational runs and calculated the linear regression formulae to transform our index measurements into the Lick system; the rms scatter of points near the linear dependencies are about 0.2 Å for all four indices under consideration, thus being within the observational errors of [17]. To correct the index measurements for the stellar velocity dispersion which is usually substantially non-zero in the centres of early-type galaxies, we have smoothed the spectrum of the standard star, HD 97907, by a set of running Gaussians of various widths; the derived dependencies of index corrections on σ were approximated by polynomials of 4th order and applied to the measured index values before their calibrations into the Lick system. Due to surface brightness differences between the circumnuclear and outer part of the bulges, the accuracy of the measured indices falls from 0.1 Å at the centre to more than 0.5 Å at the edges of the multi-pupil frame. To support a constant level of

index accuracy along the radii when analysing the stellar population properties, we co-add the individual spectra within circular rings centred onto a nucleus; the typical statistical error of the azimuthally averaged indices is 0.1 Å.

The green-range 2D spectroscopic observations are also used to cross-correlate galactic elementary spectra with a spectrum of a template star, usually of G8III–K3III spectral type, to obtain in such a way a line-of-sight velocity field for the stellar component and a map of stellar velocity dispersion. The cross-correlation peaks are fitted by Gaussians; the benefits of this approach as opposed to the more popular Fourier Correlation Quotient (FCQ) are thoroughly discussed by [20]. The red spectral range contains strong emission lines Hα and [NII]λ6583, so it is used to derive line-of-sight velocity fields for the ionized gas, mostly by calculating emission-line baricentre positions; in these particular galaxies the emission line [NII]λ6583 is the strongest, and we present only its measurements. The accuracy of elementary velocity measurements, both for stars and ionized gas, is about 10 km/s.

The second 2D spectrograph which data we use in this work is a new instrument, SAURON, operated at the 4.2 m William Herschel Telescope (WHT) on La Palma – for its detailed description see [21]. We have taken the data for NGC 3608 from the open ING Archive of the UK Astronomy Data Centre. Briefly, the field of view of this instrument is $41'' \times 33''$ with the spatial element size of $0.94'' \times 0.94''$. The sky background taken 2 arcminutes from the centre of the galaxy is exposed simultaneously with the target. The fixed spectral range is 4800–5400 Å, the reciprocal dispersion is 1.11 Å–1.21 Å varying from the left to the right edge of the frame, and the spectral resolution is about of 4 Å. The comparison spectrum is that of neon, and the linearization is made by a polynomial of the 2nd order with an accuracy of 0.07 Å. The index system is checked by using stars from the list of [17] which have been observed during the same observational run. The regressions fitting the index system calibration of the February-1999 run when NGC 3608 has been observed are shown in an earlier paper [22]. The relations between instrumental and standard-system indices are very close to the y = x relation so no corrections are needed to calibrate them into the standard Lick system. The stellar velocity dispersion effect was corrected in the same manner as for the MPFS data. Whereas to prepare the azimuthally averaged index profiles from the MPFS data, we co-added spectra in the rings, to prepare the SAURON azimuthally-averaged index data which have higher signal-to-noise ratios, we averaged the measured individual-element indices over the same rings so attached error bars are the formal rms errors of the means – they are all below 0.03 Å.

The full list of the exposures made for NGC 3607 and NGC 3608 with the two 2D spectrographs is given in table 2. The seeing was estimated by 2D-Gauss fitting of continuum images of the template stars which were observed the same nights as the galaxies under consideration.

To analyse the structure of the galaxies and to refine a kinematical analysis, for both galaxies we have retrieved the WFPC2/HST image data from the HST Archive. NGC 3607 was observed in the frame of the program of A. Phillips (ID 5999) on nuclei of S0s, and NGC 3608 was observed in the frame of the program of M. Franx on kinematically decoupled nuclei (ID 5454). For NGC 3607 we have also used the large-scale images taken from the database

Table 2. 2D spectroscopy of the galaxies studied.

Date	NGC	Exposure	Configuration	Field	Spectral range	Seeing ($FWHM_*$)
29 Apr 01	3607	45 min	MPFS+CCD $1k \times 1k$	$16'' \times 15''$	4200–5600 Å	$2.3''$
09 Mar 02	3607	45 min	MPFS+CCD $1k \times 1k$	$16'' \times 15''$	5800–7200 Å	$2.8''$
09 Mar 02	3608	60 min	MPFS+CCD $1k \times 1k$	$16'' \times 15''$	5800–7200 Å	$2.8''$
20 Feb 99	3608	120 min	SAURON+CCD $2k \times 4k$	$33'' \times 41''$	4800–5400 Å	$1.4''$

Table 3. Photometric data on NGC 3607 and NGC 3608.

Date	Galaxy	Telescope	Filter	Exposure	Seeing	Scale
7May 1994	NGC 3608	WFPC2/HST	F555W	500 s	0.1″	0.045″
7May 1994	NGC 3608	WFPC2/HST	F814W	230 s	0.1″	0.045″
6Nov 1994	NGC 3607	WFPC2/HST	F547M	260 s	0.1″	0.045″
27Jan 1996	NGC 3607	WFPC2/HST	F555W	160 s	0.1″	0.045″
27Jan 1996	NGC 3607	WFPC2/HST	F814W	160 s	0.1″	0.045″
6Feb 1999	NGC 3607	1.2-OHP	*B*	300 s	6.3″	0.686″
6Feb 1999	NGC 3607	1.2-OHP	*V*	120 s	6.0″	0.686″
6Feb 1999	NGC 3607	1.2-OHP	*R*	120 s	6.0″	0.686″
6Feb 1999	NGC 3607	1.2-OHP	*I*	120 s	5.7″	0.686″

HYPERCAT/FITS Archive (PI Ph. Prugniel). The details of the photometric observations are given in table 3.

All the data, spectral and photometric, except the data obtained with the MPFS, have been reduced with the software produced by Dr V.V. Vlasyuk in the Special Astrophysical Observatory [23]. Primary reduction of the data obtained with the MPFS was done within IDL with a software created by one of the authors (VLA). The Lick indices were calculated with our own FORTRAN program as well as by using the FORTRAN program of Dr A. Vazdekis which provides also the index error calculation.

3. Chemically decoupled cores in NGC 3607 and NGC 3608

3.1 *NGC 3607*

Figure 3 presents index maps for the central part of NGC 3607 constructed from the MPFS 2D spectral data. The Mgb map reveals a certain presence of a chemically decoupled core; this finding is not very unexpected because NGC 3607 was earlier listed by us as a good candidate for possessing a chemically distinct nucleus [24]. Interestingly, the $\langle \mathrm{Fe} \rangle \equiv (\mathrm{Fe5270} + \mathrm{Fe5335})/2$ and Hβ absorption-line index maps look rather homogeneous and do not demonstrate any sharp features. Perhaps, one can note a very shallow unresolved $\langle \mathrm{Fe} \rangle$ *minimum* near the photometric centre of the galaxy and similarly shallow extended Hβ minimum aligned with the major axis of the isophotes; the latter feature may be associated to the circumnuclear ionized-gas disk mentioned in the Introduction and probably results from the emission contamination of the Hβ absorption line. However, both $\langle \mathrm{Fe} \rangle \equiv (\mathrm{Fe5270} + \mathrm{Fe5335})/2$ and Hβ absorption line index minima are marginal, and the Mgb peak is much more prominent than the other details. It seems to be resolved; moreover, it seems to be elongated along the minor axis of the isophotes. To clarify the orientation of the magnesium-enhanced core, we have smoothed strongly the Mgb map and have drawn isolines of the smoothed Mgb distribution (figure 3, top right). Indeed, the magnesium-enhanced core is elongated in $PA \approx 46^\circ$ though the Mgb isolines do not look quite symmetric ovals. The orientation of the magnesium-enhanced area hints at some stellar substructure, which may be seen with its alignment along the minor axis of the isophotes, some kind of minibar. But in fact, the Mgb-index distribution morphology alone is not enough to draw conclusions about the nature of the magnesium-enhanced core: the visible elongation of the magnesium-enhanced core may be a result of a magnesium depression along the major axis, similar to that of the Hβ index, which may be caused by a very young stellar disk aligned with the major axis. To draw definite conclusions, further analysis of the stellar population age in an area of the magnesium-enhanced core is needed.

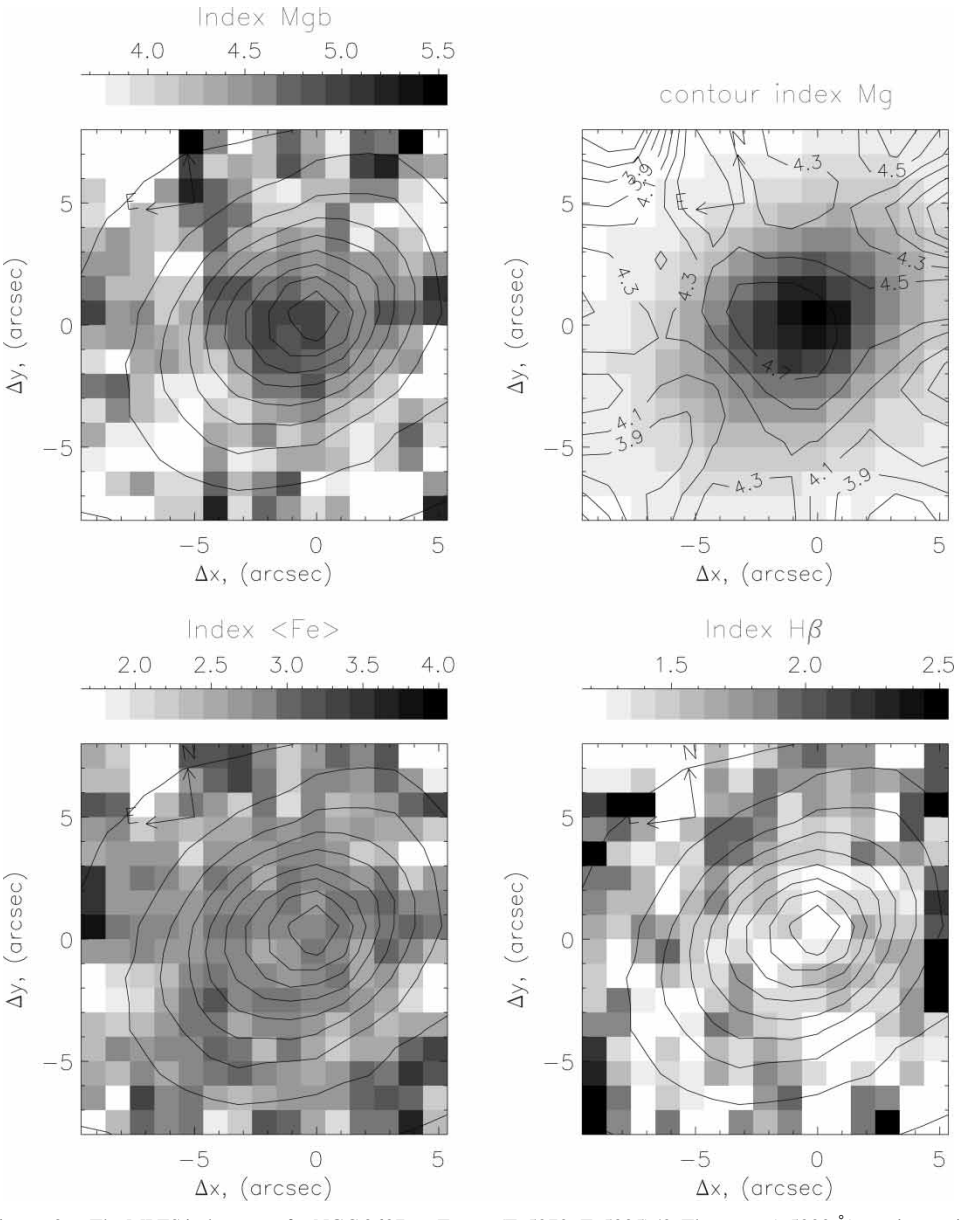

Figure 3. The MPFS index maps for NGC 3607; $<$ Fe $>\equiv$(Fe5270+Fe5335)/2. The green (λ5000 Å) continuum is overlaid by isophotes in three plots from four. At the right top the Mgb index distribution smoothed strongly with the 2D Gaussian of $FWHM = 3.5''$ is plotted by isolines to show an orientation of the chemically decoupled structure; here the green continuum is gray-scaled.

To quantify peculiarities of the absorption-line index distributions in the centre of NGC 3607 seen in figure 3, we have calculated azimuthally averaged radial profiles of the indices and have compared them to the 'zero-dimensional' and one-dimensional spectral data published in the literature [25], [26], and [27]) (figure 4). Though the long-slit data were taken along the major or minor axis of NGC 3607 and so were not obliged to agree exactly with our azimuthally averaged measurements, they confirm the overall shape of the index radial dependencies: a rather flat iron-line profile, an Hβ profile with a shallow minimum in the centre, and a

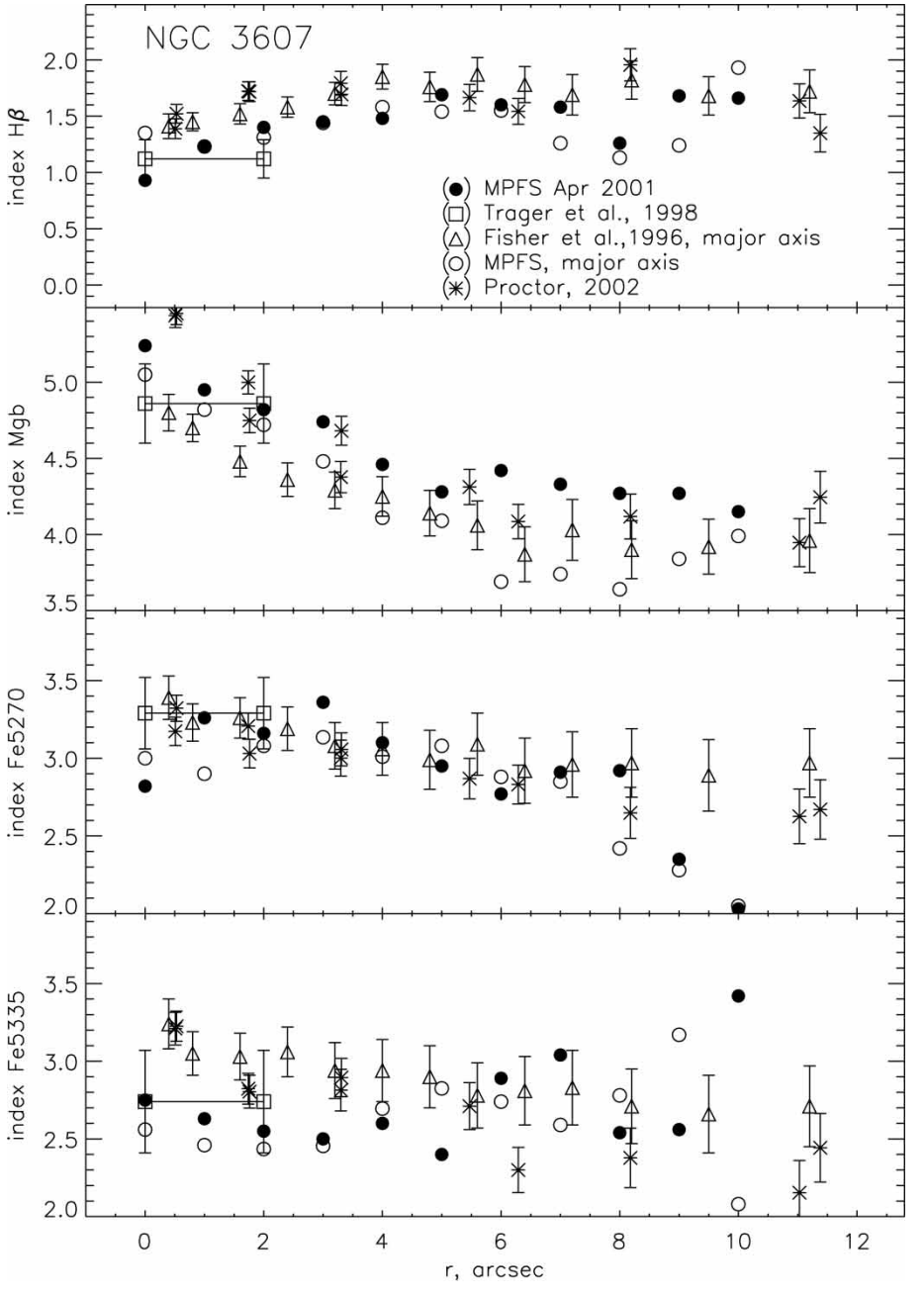

Figure 4. The MPFS azimuthally-averaged index profiles for NGC 3607 in comparison with the literature data. The minor-axis long-slit cross-section by [25] is plotted. The long-slit data taken along the major axis by [27] are also confronted to the major-axis index profiles simulated from our 2D index maps with the digital slit width of $2''$. The central $4''$-aperture measurements by [26] are plotted as connected squares at $R = 0'' - 2''$.

magnesium-distinct core with the radius of $5'' - 6''$. A moderate, of 0.2 Å–0.4 Å, systematic discrepancy of our Hβ and Mgb profiles with the data of [27] can also be noted. To check if these shifts may result from lack of azimuthal symmetry, we simulated one-dimensional major-axis cross-sections of our index maps and also plotted the simulated results in figure 4.

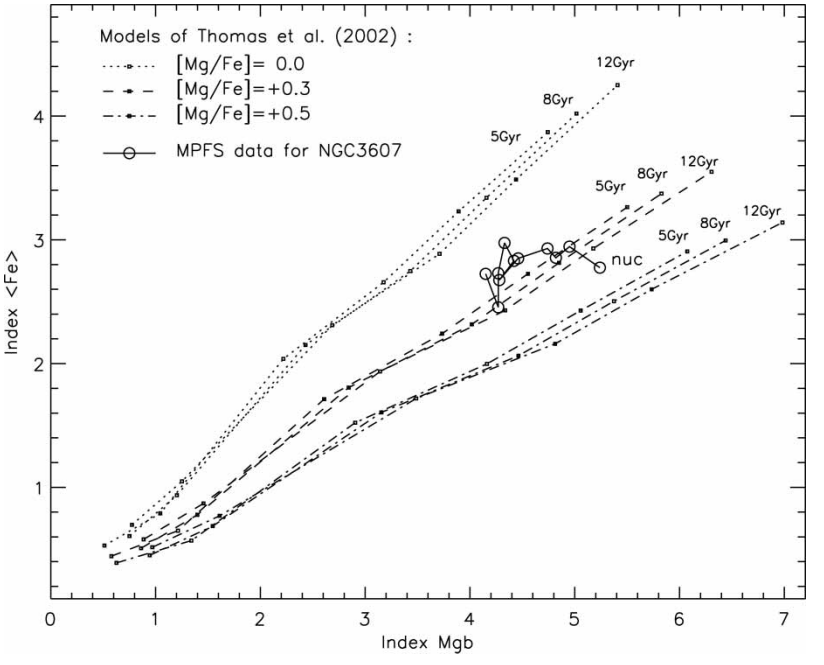

Figure 5. 'Index-index' < Fe > vs Mgb diagnostic diagram for the azimuthally averaged Lick indices in the centre of NGC 3607 taken along the radius with the step of 1″ (open circles connected by a thin line, the nucleus being marked as 'nuc'). The errors of the azimuthally averaged MPFS indices are about 0.1 Å. The models for [Mg/Fe] = 0.0, +0.3, and +0.5 are plotted as a reference frame; the small signs connected by pointed, dashed, and point-dashed lines represent stellar population models of equal ages; the metallicities for the models are +0.67, +0.35, 0.0, −0.33, −1.35, and −2.25 if one takes the signs from top to bottom.

Indeed, the simulated major-axis Mgb profile has a much better agreement with the Fisher et al.'s data than the azimuthally averaged measurements. As for the Hβ index profiles, the simulated major-axis profile and the azimuthally averaged one have coincided almost perfectly, implying an orientation of the ionized-gas disk far from edge-on, so we must conclude that the systematic shift of ∼0.2 Å between our measurements and those of [25] and [27] exists. Meantime, the centred aperture measurement of [26], which may be treated as a Lick-system etalon, confirms our calibration.

Due to progress in evolutionary population synthesis during recent years, we can now estimate mean stellar population characteristics by comparing different absorption-line indices with each other. Figure 5 presents an 'iron-vs-magnesium' diagram where we compare our azimuthally averaged MPFS data for the central part of NGC 3607 with the models of [28], which are calculated for several values of magnesium-to-iron ratio. The loci of the models of various [Mg/Fe] are well separated on the diagram, so from inspecting figure 5 we can conclude that the magnesium-to-iron ratio in the centre of NGC 3607 is certainly above the solar one. But whereas in the circumnuclear region the [Mg/Fe] is between zero and +0.3, perhaps, closer to +0.2, the unresolved nucleus is outstanding with its [Mg/Fe] ≈ +0.4. We must note that, as figure 4 demonstrates, the previous Lick index measurements for the centre of NGC 3607 do not confirm this jump of [Mg/Fe] at $R = 0''$ and imply rather constant iron-index behaviour along the radius. Since our estimates of the nuclear indices are confined to a single spatial element, we cannot insist that the low Fe5270 value in the unresolved nucleus is not a random artefact. So over the whole of the centre of NGC 3607 we assume the [Mg/Fe] ratio to be between +0.2 and +0.4.

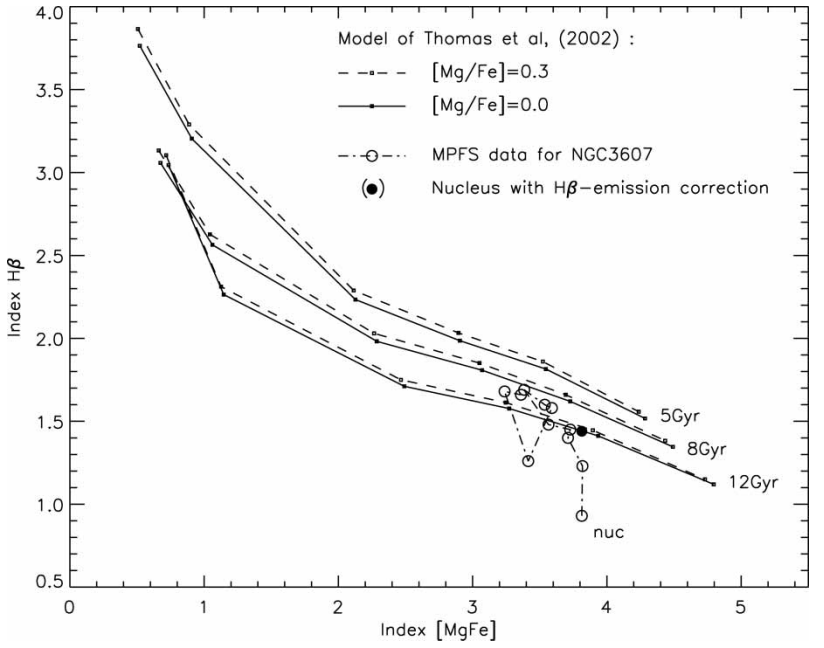

Figure 6. 'Index-index' Hβ vs [MgFe], [MgFe]$\equiv$ (Mgb $<$ Fe $>$)$^{1/2}$, age-diagnostic diagram for the azimuthally averaged Lick indices in the centre of NGC 3607 taken along the radius with the step of 1″ (open circles connected by a dot-dashed line, the nucleus being marked by 'nuc'). The errors of the azimuthally averaged MPFS indices are about 0.1 Å. The models for [Mg/Fe] = 0.0 and +0.3 are plotted as a reference frame; the small signs connected by solid and dashed lines represent stellar population models of equal ages; the metallicities for the models are +0.67, +0.35, 0.0, −0.33, −1.35, and −2.25, if one takes the signs from the right to the left.

Several investigators, e.g. [29] or [30], noted that in order to overcome an effect of the non-solar magnesium-to-iron ratio when determining a mean age of stellar population, one must use a combined index [MgFe] $\equiv$ (Mgb$\langle$Fe$\rangle$)$^{1/2}$. So in figure 6 we confront [MgFe] to Hβ?? and compare our azimuthally averaged data for NGC 3607 with two sets of the models – for [Mg/Fe] = 0 and for [Mg/Fe] = +0.3. As promised by our choice of the metal-line index, the age estimates are robust to the varying choice of the model [Mg/Fe]; they are equal to about 10–12 Gyr. The nucleus is again outstanding, probably, due to the Balmer emission concentration in the very centre of the galaxy and obvious Hβ emission contamination; but beyond the nucleus the age gradient along the radius is non-detectable: at the diagram 'Hβ, [MgFe]' the index variations occur along the model sequence of equal age, namely, of $T = 10 \pm 2$ Gyr. We may suspect that the real mean age of the stellar population in the centre of NGC 3607 is lower than 12 Gyr, because the ionized-gas disk is known to extend up to $R \approx 15''$ ([10], [11]) and therefore the Balmer emission contaminates the absorption-line Hβ index to some degree all the way. In the nucleus this effect must be especially strong, and we would try to correct it there by using measurements of the Hα-emission equivalent width by [31]. To correct the measured Lick index Hβ for the emission Hβ we use the well-known fact that an emission line Hα is always much stronger than Hβ and an absorption line Hα is always weaker than Hβ, so the equivalent width of the emission line Hα can be measured more precisely than that of Hβ. The authors of [31] subtracted a pure-absorption template from the observed nuclear spectrum and obtained $EW(\mathrm{H}\alpha\, emis) = 2.03$ Å for NGC 3607; note here that in the nucleus of NGC 3608, another target galaxy, they saw only a marginal Hα emission, less that $EW = 0.4$ Å. The well-established and minimum possible intensity ratio Hα/Hβ is known for the case of the gas radiative excitation by OB-stars ('HII-region'-type excitation),

2.5–2.7, and it is much larger for shock excitation. The authors of [31] classified the nuclear emission spectrum of NGC 3607 as a LINER. In [32] a large sample of integrated spectra of galaxies of various morphological types has been analysed, and it has been found that a good correlation $EW(\mathrm{H}\beta\ emis) = 0.25EW(\mathrm{H}\alpha\ emis)$ exists; just the relation we use to calculate $EW(\mathrm{H}\beta\ emis)$, which is in fact the correction of the Lick index Hβ for the emission. After it has been corrected for the emission contamination of the Hβ index, the nucleus of NGC 3607 has settled to the age sequence of 12 Gyr in the figure 6, and any age difference between the nucleus and its outskirts has disappeared. We would like to stress that any significant age break is also absent at the border between the magnesium-enhanced core of NGC 3607 and its 'bulge', at $R = 5'' - 6''$.

3.2 *NGC 3608*

Figure 7 presents the index maps for NGC 3608, similar to those presented for NGC 3607 in figure 3, but calculated from the SAURON data, so instead of the combined iron index $\langle \mathrm{Fe} \rangle \equiv (\mathrm{Fe5270} + \mathrm{Fe5335})/2$ we give here the Fe5270 surface distribution. We note a qualitative resemblance of the index distributions in both galaxies: just as we have seen in NGC 3607, in

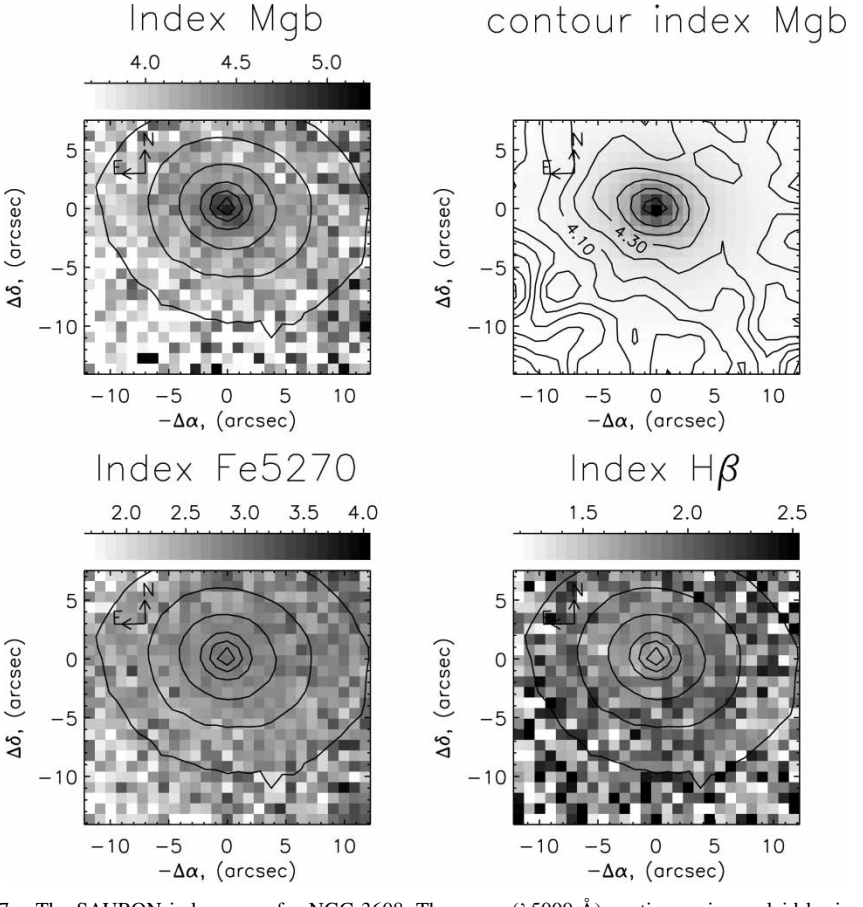

Figure 7. The SAURON index maps for NGC 3608. The green (λ5000 Å) continuum is overlaid by isophotes in three plots from four. At the top right the Mgb index distribution smoothed strongly with the 2D Gaussian of $FWHM = 3.5''$ is plotted by isolines to show an orientation of the chemically decoupled structure; here the green continuum is gray-scaled.

its elliptical neighbour the magnesium index demonstrates a prominent extended peak in the centre, and the iron index shows a flat, homogeneous distribution. However, the isolines of the smoothed Mgb distribution (figure 7, top right) are elongated in $PA \approx 75°$, or along the global major axis of NGC 3608 (see table 1), conversely to NGC 3607 where the magnesium isolines are aligned with the minor axis of the isophotes. This fact, together with a high ellipticity of the Mgb isocontours within $R \approx 5''$, 0.33, which exceeds the isophote ellipticity anywhere in the galaxy, $1 - b/a \leq 0.2$, gives some evidence in favour of the chemically decoupled core treatment as a circumnuclear disk.

In figure 8 we present azimuthally averaged index profiles and their comparison with the literature data. The shapes of the profiles are qualitatively similar to those in NGC 3607 (figure 4). Perhaps, the magnesium-enhanced core is somewhat more compact: we would put its border at $R \approx 5''$. The break of the Mgb-profile slope at this radius is rather evident: between $R = 0''$ and $R = 4.7''$ the Mgb index changes by 0.8 Å, whereas beyond $R = 5''$ an approximation of the azimuthally-averaged measurements by a linear fit gives the slope

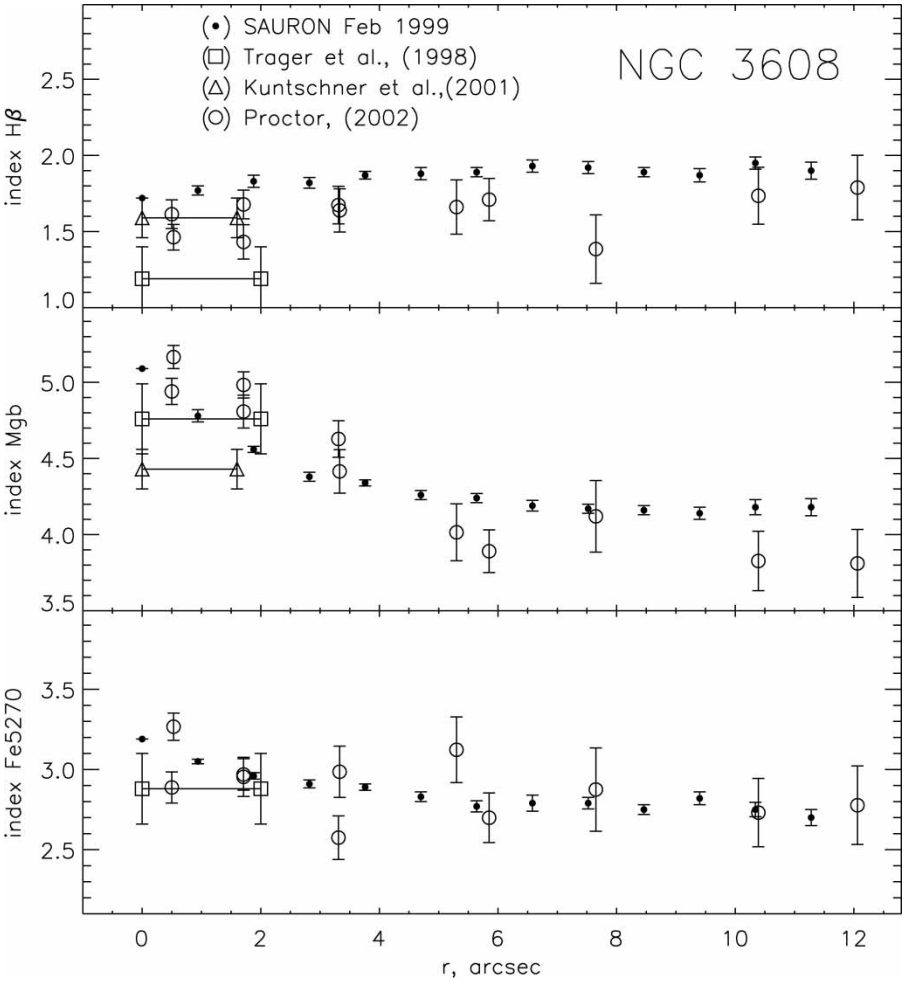

Figure 8. The SAURON azimuthally averaged index profiles for NGC 3608 in comparison with the literature data. The minor-axis long-slit data of [25] are plotted. The aperture measurements by [26] and by [33] are also plotted as connected squares and triangles at $R = 0'' - 2''$.

of -0.008 ± 0.006 Å per arcsec, or almost negligible, and a zero-point of 4.222 ± 0.047 Å – compare to the measured central Mgb value of 5.00 Å. Let us recall that the maximum rotation velocity of the counterrotating core is also achieved near $R \approx 4''$ [13], so in the case of NGC 3608 we deal with a dynamically *and* chemically decoupled core, just as in the case of another elliptical galaxy NGC 4365 [34]. The Fe5270 measurements are in good agreement with the minor-axis long-slit data of [25] and with the central aperture data of [26], so we may conclude that in the SAURON data of February 1999 for NGC 3608 the systematic offset of the Fe5270 calibration by 0.4 Å seen in the later data, e.g. for NGC 3384 ([35], [1]), is probably absent. However, in this case there may be a small systematic shift, by some +0.2 Å, of the Hβ calibration.

With these azimuthally averaged index profiles, we would try to estimate radial variations of the characteristics of the stellar population in the centre of NGC 3608 by using index–index diagrams. In figure 9 (*top*) we compare the SAURON data on the index radial variations with the models of [28] for various [Mg/Fe] at the diagram 'Fe5270, Mgb'. It is clearly seen that the radial variation of the magnesium-to-iron ratio in the centre of NGC 3608 is negligible, and both the chemically decoupled core and its outskirts have [Mg/Fe]$\approx +0.3$. So to determine a mean stellar age in this galaxy, we must take the models with just this magnesium overabundance. Figure 9 (*bottom*) shows the comparison of the azimuthally averaged index

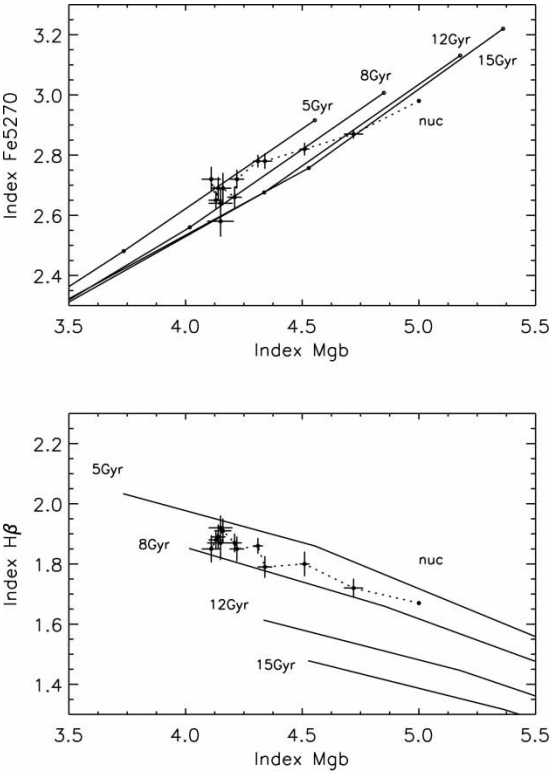

Figure 9. 'Index-index' diagnostic diagrams for the azimuthally averaged Lick indices in the centre of NGC 3608 taken along the radius with the step of 0.94″ (solid points connected by a dashed line, the nucleus being marked by 'nuc'); *(top)* **Fe5270 vs Mgb** diagram, with the models of [28] for [Mg/Fe] = +0.3, and *(bottom)* **Hβ vs Mgb**, with the same model set. Small signs in the top plot connected by solid lines belong to stellar population sequences of equal ages, particularly, of 5 Gyr, 8 Gyr, 12 Gyr, and 15 Gyr from top to bottom; their metallicities are +0.35 and 0.00, if one takes the signs from the right to the left.

data for NGC 3608 with the models of [28] at the diagram 'Hβ, Mgb'. Again, as in the case of NGC 3607, we cannot detect any age gradient along the radius: the data sequence follows the model sequence of equal age, this time it lies between the model age sequences of $T = 5$ Gyr and $T = 8$ Gyr. Since the emission lines are very weak in the centre of NGC 3608 (in particular, we have failed to detect [OIII]λ5007 emission line in the green SAURON spectra), we think that this age estimate, $T = 6 - 7$ Gyr, is close to the real value. Similarly to NGC 3607, the data for NGC 3608 does not reveal any age break at the transition point from the magnesium-enhanced core to the rest of the galaxy. The moderate metallicity difference of $\Delta \log Z \approx +0.2$ is, however, detected between the nucleus, $R = 0''$, and the 'non-core' stellar body, $R > 4''$ (figure 9, *bottom*).

Let us to note that if the systematic shift of the Hβ calibration by some 0.2 Å is real, this would result in the age underestimation by some 4 Gyr. Similarly, if for NGC 3607 the Hβ index calibration by [27] and [25] is more correct than ours, it would mean that we overestimate the mean stellar age in the centre of NGC 3607 by the same 4 Gyr. So we do not insist on the absolute values of the age estimates obtained here. The main result of this consideration is the relative age estimates, namely, that there are no noticeable age variations along the radii within some $10''$ in both galaxies, and particularly, there are no age drop or rise at the borders of the magnesium-enhanced cores.

4. Stellar and gaseous kinematics and the structure of the central kiloparsecs

Since the integral-field spectroscopy provides us with 2D line-of-sight velocity fields, we are able now to analyse both character of rotation and central structure of the galaxies. If we have an axisymmetric mass distribution and bulk rotation on circular orbits around the symmetry axis, the direction of maximum central line-of-sight velocity gradient (we shall call it 'a kinematical major axis') should coincide with the line of nodes of the main symmetry plane as well as the photometric major axis should do; whereas in the case of a triaxial potential the isovelocities would tend to align with the principal axis of the ellipsoid [36] and generally the kinematical and photometric major axes would diverge, showing the turns with respect to the line of nodes in opposite senses if the main axis of the triaxial potential is not strictly aligned with the line of nodes ([37], [38]). In the simplest case of thin-disk rotation we have a convenient analytical expression for the azimuthal dependence of the central line-of-sight velocity gradients within the area of solid-body rotation:

$$\frac{dv_r}{dr} = \omega \sin i \cos(PA - PA_0),$$

where ω is the deprojected central angular rotation velocity, i is the inclination of the rotation plane, and PA_0 is the orientation of the line of nodes of the rotation plane. In more complex three-dimensional case the validity of the formula above is not so evident; however the observed dependencies of dv_r/dr on PA also look cosine-like as one can see in figures 10 and 11. Perhaps, it results from symmetry properties that vertical and radial velocity components vanish due to integration along the line of sight. At least it is widely-known that axisymmetric oblate spheroids demonstrate zero line-of-sight velocity gradients along their minor axes [39] and the maximum rotation along their major axes [40]. So by fitting azimuthal variations of the central line-of-sight velocity gradients by a cosine law, we can check the axisymmetry of the mass (star?) distribution and determine the orientation of the kinematical major axis by its phase and the central angular rotation velocity by its amplitude. It is our main tool for kinematical analysis.

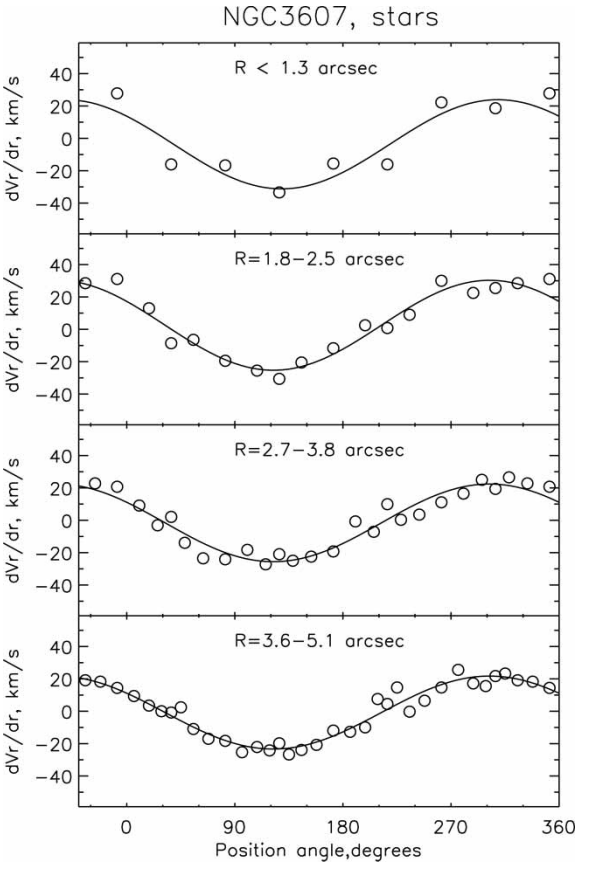

Figure 10. The azimuthal dependencies of the central stellar line-of-sight velocity gradients taken in several radial bins for NGC 3607 according to the MPFS 2D velocity measurements.

4.1 *NGC 3607*

Figure 12 presents kinematical maps for the central part of NGC 3607. Both stars and ionized gas demonstrate regular, almost rigid-body rotation with their kinematical major axes close to the photometric major axis. The gas rotation, though slightly asymmetric, is twice as fast as that of the stars: the central angular rotation velocity is $\omega_{gas} \sin i \approx 50$ km/s/arcsec whereas $\omega_{stars} \sin i \approx 28$ km/s/arcsec. Note that if the inclination given by LEDA for the symmetry galactic plane, 34° (table 1), is correct, it means that the gas rotates at a speed of 800 km/s/kpc. However, below we should recognize that it is rather difficult to determine precise orientation(s) of the rotation plane(s) in the centre of NGC 3607. The stellar velocity dispersion has a peak near the nucleus; in our data this stellar velocity dispersion maximum area is not exactly centred onto the nucleus and seems to be extended in the direction of the isophote minor axis.

To check our 2D mapping of the line-of-sight velocities, we have simulated one-dimensional cross-sections of the velocity fields of figure 12 and have compared the simulated LOS velocity and stellar velocity dispersion profiles with the long-slit data along the major axis of NGC 3607, which we have found in the literature (figures 13 and 14). One can see that the agreement of the velocity profiles is rather good. However, the literature data do not support the shift of the velocity dispersion peak with respect to the photometric centre found by us;

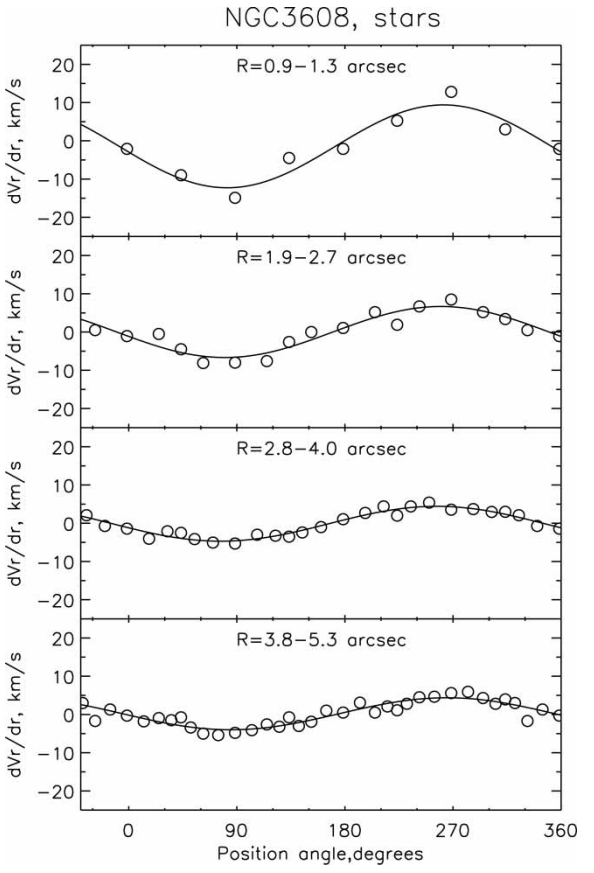

Figure 11. The azimuthal dependencies of the central stellar line-of-sight velocity gradients taken in several radial bins for NGC 3608 according to the SAURON 2D velocity measurements.

here we would like to stress that 2D spectroscopy has far less problems with positioning one-dimensional kinematical cross-sections than the long-slit spectroscopy. Also, perhaps the slope of the ionized gas velocity profile in our data may be slightly underestimated due to moderate seeing quality of the observations of March 2002. The maximum gas rotation velocity, $\sim$250 km/s at $R = 5'' - 10''$ which may be transformed into 450 km/s under $i = 34^\circ$, seems to be enormous; but this result is confirmed by very recent CO observations of NGC 3607 according to which $2.3 \cdot 10^8 M_\odot$ of the molecular gas within $R = 5''$ rotates at a speed of 250 km/s [43]. Interestingly, in the integrated molecular-line profile only a receding horn is well seen – the asymmetry is quite similar to that of figure 12 (the lower left). The stellar velocity profile of figure 13 reveals a prominent rotation velocity maximum at $R \approx 6''$ after which the rotation velocity drops by a factor of $\sim$3 toward $R = 20'' - 25''$. Such behaviour allows one to detect a kinematically distinct area in the centre of NGC 3607; note that the maximum rotation radius coincides exactly with the border of the magnesium-enhanced structure (see the previous section).

The enormous rotation velocity, which we have measured in the centre of NGC 3607 and which implies a mass concentration of more than $10^{10} M_\odot$ within $R \approx 0.5$ kpc, provokes some doubts about a circular (axisymmetric) character of rotation. We can check it by comparing kinematical and photometric major axis orientations; it is done in figure 15. Our first impression from inspecting figure 12 is that the kinematical and photometric major axes coincide; figure 15

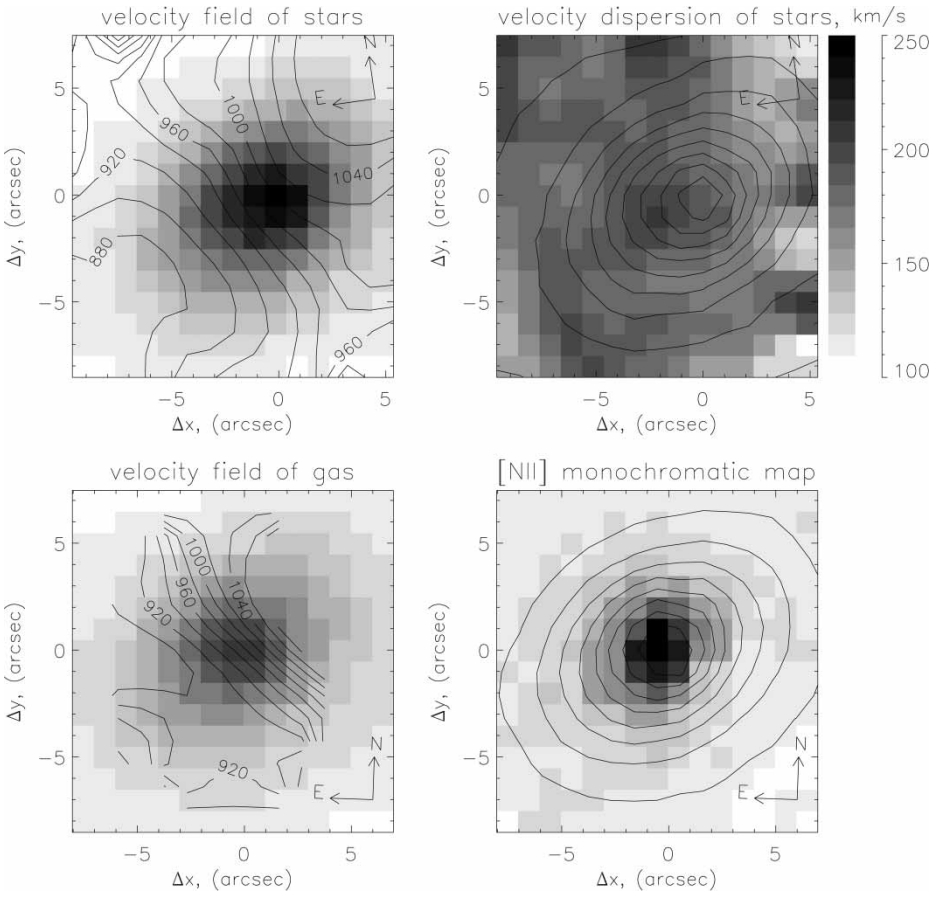

Figure 12. The line-of-sight velocity fields of the stellar component (top left) and of the ionized gas (bottom left), and the stellar velocity dispersion map (top right) and the [NII] emission line intensity distribution (bottom right, gray-scaled) in the central part of NGC 3607. The continuum intensities, in the green for the stars and in the red for the gas, are overlaid by isophotes.

confirms this impression by quantifying it. At $R > 3''$, or more exactly at $R = 3'' - 6''$, within the decoupled core area, the kinematical major axes of the ionized gas and of the stars, as well as the photometric major axes of the continuum brightness distribution are all close to the global line of nodes of the galaxy, $PA_0 = 300°(120°)$. This fact agrees with a picture of axisymmetric gas and star rotation with the spin orthogonal to the main symmetry plane of the galaxy – a classic configuration corresponding to the SA0-type of NGC 3607. But inside $R = 2''$ ALL THE AXES – both the kinematical ones and the photometric one – seem to turn toward larger PAs, the turn of the gas kinematical major axis being the most prominent. We have estimated an orientation of the innermost isophotes of Hα + [NII] emission distribution in figure 1f of [10] – it is $PA \approx 325°$, very close to our measurements of the [NII] emission-line brightness distribution elongation; the gray-scaled emission map provided by [11] confirms also the turn of the innermost gas emission isophotes toward larger PAs. The coincidence of the photometric major axes and of the kinematical major axis of the ionized gas at $PA \approx 325°$ means an axisymmetric structure, but the rotation plane of the innermost, $R < 2''$, part of the galaxy (of a circumnuclear disk?) is obviously inclined to the main symmetry plane of NGC 3607, whereas the more outer gas rotates in the global galactic plane together with the stars. The latter fact excludes an external origin of the decoupled central spin; there must

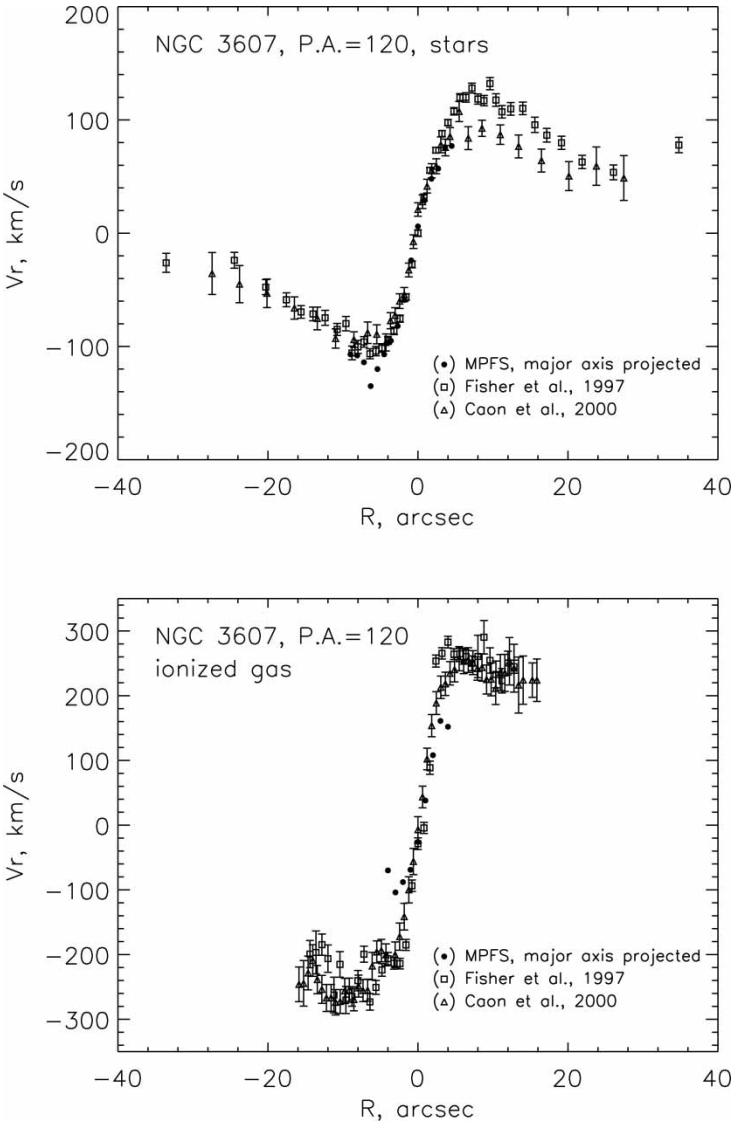

Figure 13. The comparison of the line-of-sight velocity variations simulated along the major axis by using our 2D velocity fields for the stars and ionized gas in NGC 3607 with the literature data of [40] and of [41]. The slit width used in the simulations is 2″.

be own peculiarities of NGC 3607 to provide such kinematical appearance. Figure 16 shows radial variations of the isophote characteristics in NGC 3607 at larger scales than figure 15 does. The isophote major axis position angle remains almost constant all along the radius. But the ellipticity behaviour is indeed strange: it reaches a main maximum of 0.3 at the border of the decoupled core, at $R = 6''$, then it reaches a secondary maximum of 0.2 at $R \approx 20''$, and after that it falls to $1 - b/a \approx 0.1$ at $R \approx 60''$. The tabular inclination of the global galactic disk, $i = 34°$ (LEDA), corresponds only to $1 - b/a = 0.17$ for a case of infinitely thin disk. Let us also to note that the radius of the minimal ellipticity, $R \approx 60''$, coincides with the boundary between the bulge and the global disk of NGC 3607: according to [44], in NGC 3607 the bulge dominates at $R < 60''$ and the exponential disk – at larger radii. The

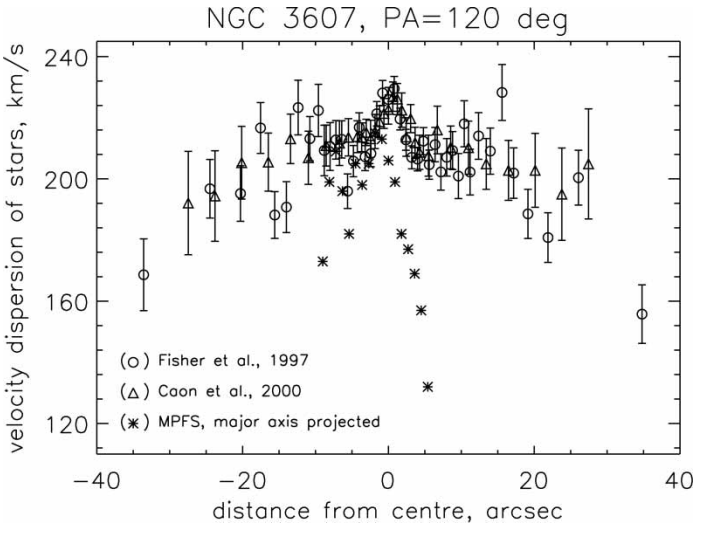

Figure 14. The comparison of the stellar velocity dispersion variations simulated along the major axis by using our 2D velocity fields for the stars and ionized gas in NGC 3607 with the literature data of [40] and of [41]. The slit width used in the simulations is 2″.

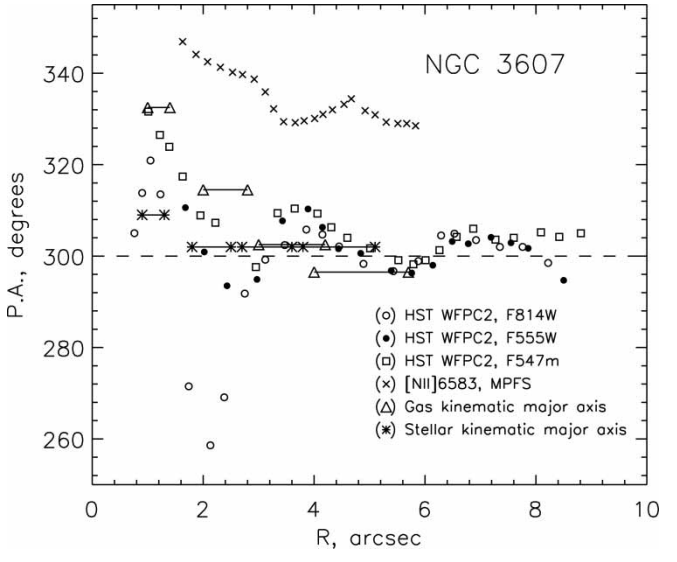

Figure 15. Isophote major axis position angle compared to the orientations of the kinematical major axes (see the text) for the stars and ionized gas in the centre of NGC 3607. The errors of the kinematical major axes determination are estimated as 1–1.5 deg. The line of nodes determined from the outermost disk isophote orientation, $PA = 300°$, is traced by a dashed line.

ellipticity behaviour at $R \geq 20''$ is rougly consistent in all filters, so it is not effect of dust. We must conclude that the bulge of NGC 3607 cannot be an axisymmetric (oblate) spheroid if require that its symmetry plane must coincide with the disk plane, otherwise its visible ellipticity should be smaller than that of the more thin disk; it may be triaxial at a scale of a few kiloparsec.

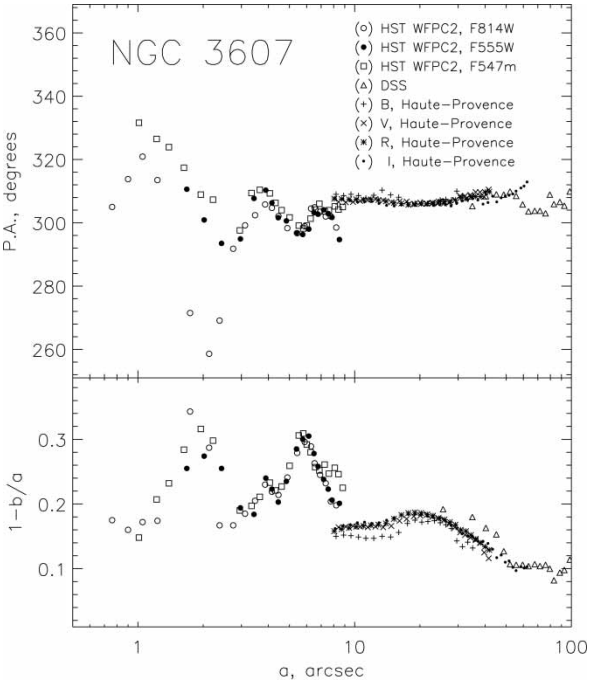

Figure 16. Isophote characteristics for the full radius range of NGC 3607.

4.2 *NGC 3608*

Figure 17 presents kinematical maps for NGC 3608: the stellar line-of-sight velocity field and the stellar velocity dispersion map according to the SAURON data, as well as the gas velocity field and the nitrogen emission brightness distribution according to the MPFS data. The SAURON kinematical maps for NGC 3608 are already published by [45] together with the maps of the LOSVD higher moments h_3 and h_4; the qualitative agreement of our kinematical results obtained independently from the raw SAURON data and those of [45] is perfect. However, the detailed analysis of the structure of the kinematically decoupled core in NGC 3608 has not yet been presented. In figure 17 (top left) one can look at a 2D view of this kinematically decoupled core. It reveals indeed a regularly counterrotating stellar subsystem with the kinematical major axis close to the major axis of the inner isophotes. The stellar velocity dispersion has a maximum in the centre, with a weak elongation of the high-dispersion area along the major axis – this fact restricts strongly the possible scenario of the counterrotating core origin. The ionized-gas velocity field (figure 17, bottom left) reveals a strong twist of the isovelocites over the whole measured velocity field. The amplitude of the circumnuclear azimuthal variations of the gas line-of-sight velocity gradient is 73 ± 15 km/s/arcsec – even higher than in NGC 3607. The phase of the cosine curve fitting the circumnuclear azimuthal variations of the gas line-of-sight velocity gradient within $R = 2''$ is shifted by $\sim 70^\circ$ with respect to the line of nodes of the stellar rotation. Since the nucleus of NGC 3608 is inactive and radio-quiet, we would disregard a hypothesis of outflow and would claim rather a kind of strongly inclined gaseous ring with a radius of $\sim$200 pc. In figure 18 we compare the orientations of the kinematical and photometric major axes, for the stars and for the ionized-gas emission [NII]λ6583. The kinematical and photometric axes of the stellar component are in agreement that implies an axisymmetric rotation; but both major axes, at $R = 3'' - 4''$ being

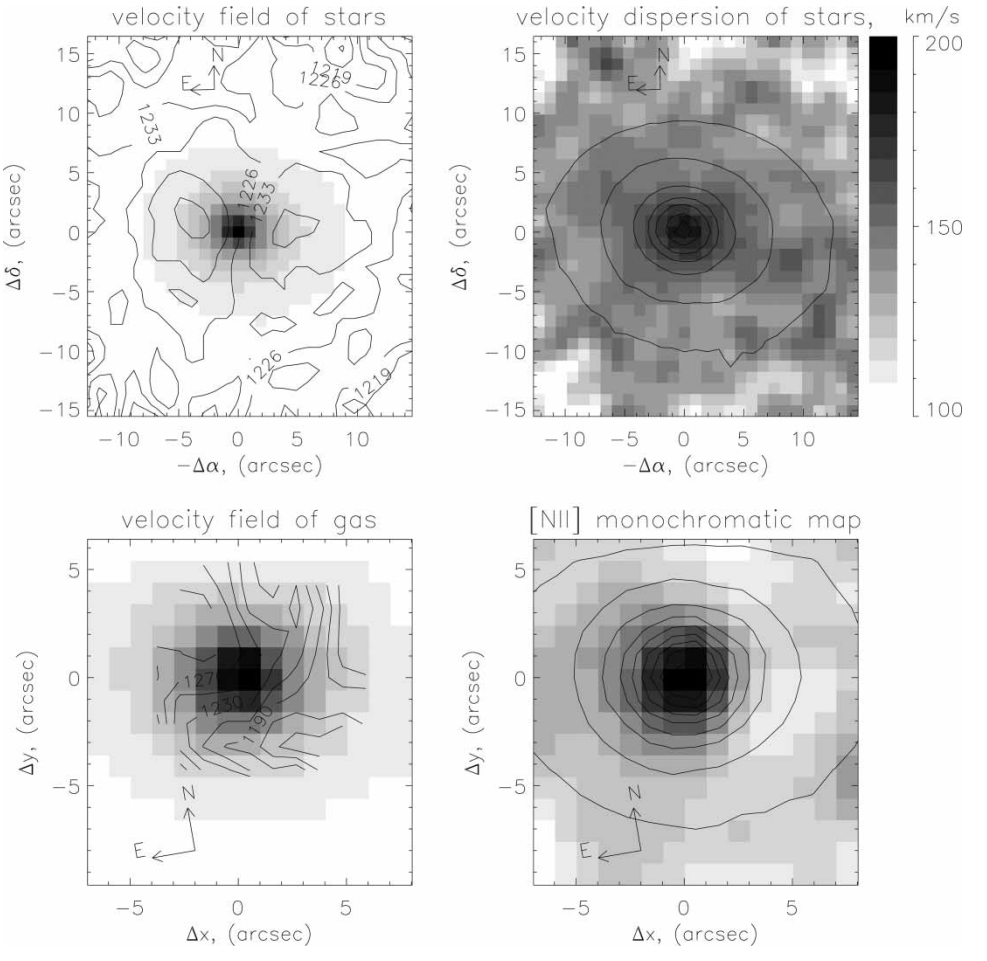

Figure 17. The line-of-sight velocity fields of the stellar component (top left) and of the ionized gas (bottom left), and the stellar velocity dispersion map (top right) and the [NII] emission line intensity distribution (bottom right, gray-scaled) in the central part of NGC 3608. The continuum intensity, in the green for the stars and in the red for the gas, are overlaid by isophotes.

practically coincident with the PA of outer isophotes, $PA_0 = 75°$, turn systematically when approaching the very centre. Meantime, the major axes of the [NII] emission brightness distribution and of the ionized-gas velocity field are again in agreement with each other that implies a stable regular disk rotation, but both axes are turned strongly with respect to the stellar configuration at $R < 4''$, or within the kinematically decoupled area. The spatial resolution of our red MPFS observations is rather moderate, so the measurements inside $R = 2.5''$ are strongly affected by the seeing effect. From the published HST data analysis [46] we know that in the centre of NGC 3608 the dust ring with a radius of $0.5''$ is roughly aligned with the outer-isophote orientation, $PA_{dust} \approx 80°$ (see also our figure 2, right plot); as the dust and the gas are related, the orientation of the circumnuclear gas plane must also be close to the line of nodes, so one may extrapolate our measurements back to the line of nodes inside $R \approx 1''$. Strong twist of both the photometric and kinematical major axes for the gas component at $R = 1'' - 4''$, though being obviously smoothed by the seeing effect, implies neverthless the existence of a kind of polar gas rotation in the above-mentioned radius range.

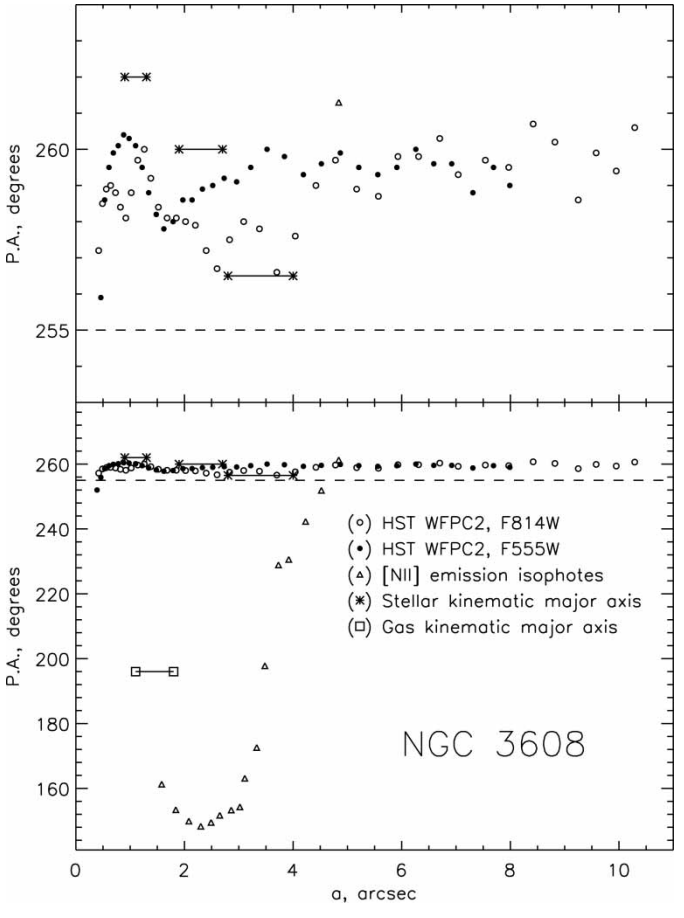

Figure 18. Isophote major axis position angles compared to the orientations of the kinematical major axes (see the text) for the stars and ionized gas in the centre of NGC 3608. The line of nodes determined from the outermost isophote orientation, $PA = 255°$, is traced by a dashed line. The data for the stars are zoomed separately at the top plot to demonstrate the kinematic major-axis turn. The errors of the kinematical major axes determination are estimated as 1–1.5 deg.

Figures 19 and 20 demonstrate simulated major- and minor-axis cross-sections of the stellar velocity and velocity dispersion field in comparison with published long-slit data. The agreement of our cuts with the literature long-slit data is satifactory though the systematic shift of our stellar velocity dispersion measurements by $\sim -30 - -40$ km/s can also be seen. Note that systematic differences of a few dozen kilometre per second are still common in stellar velocity dispersion measurements; for example, in the recent study of 48 early-type galaxies [45] the differences between measured central-aperture stellar velocity dispersions and literature data reaches 40 km/s in some cases. Moreover, in [47] it has been shown that even using the same method to measure σ_* over data of similar quality but in different spectral bands, the stellar velocity dispersion estimates may differ by 20–30 km/s. So we would not refer to the absolute values of σ_* but rather analyse their relative variations over the field of view. Besides the overall check of the quality of our velocity measurements, these figures 19 and 20 confirm once more that the border of the kinematically decoupled stellar core is located at $R = 4''$ and, therefore, coincides roughly with the border of the magnesium-decoupled core. But, conversely to the results of the analysis of the stellar population properties, the kinematical analysis does not

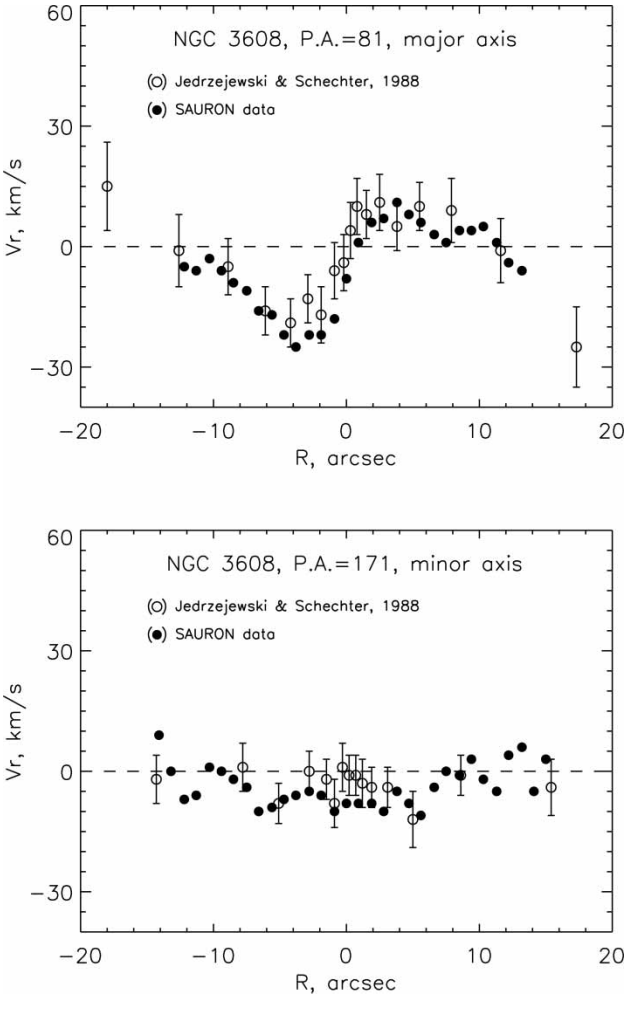

Figure 19. The comparison of the line-of-sight velocity profiles simulated along the major and minor axes by using the SAURON 2D velocity field for the stars in the centre of NGC 3608 with the literature data of [13]. The slit width used in the simulations is 2″.

leave a possibility to treat the decoupled core as a compact stellar disk. The low v/σ ratio and a pattern of the stellar velocity dispersion distribution – the extended maximum elongated along the major axis – allow the suggestion of triaxiality of the decoupled core. In such a configuration the polar rotation of the ionized gas becomes explicable: we often meet circumnuclear polar gaseous disks in galaxies with triaxial bulges or within bars – e.g. in NGC 2841 ([48], [49]), in NGC 6340 [50], in NGC 7280 [51], in NGC 4548 [52], etc.

5. Discussion

As a result of a thorough study of the central regions of the brightest and the nearest to the centre galaxies of the Leo II group, we note a kinematically distinct area in the centre of NGC 3607 – although a fall of the rotation velocity after the circumnuclear maximum at $R = 6''$ was earlier reported by [41] – and confirm a presence of the counterrotating core in NGC 3608. Both kinematically decoupled cores have appeared to be also distinguished by a

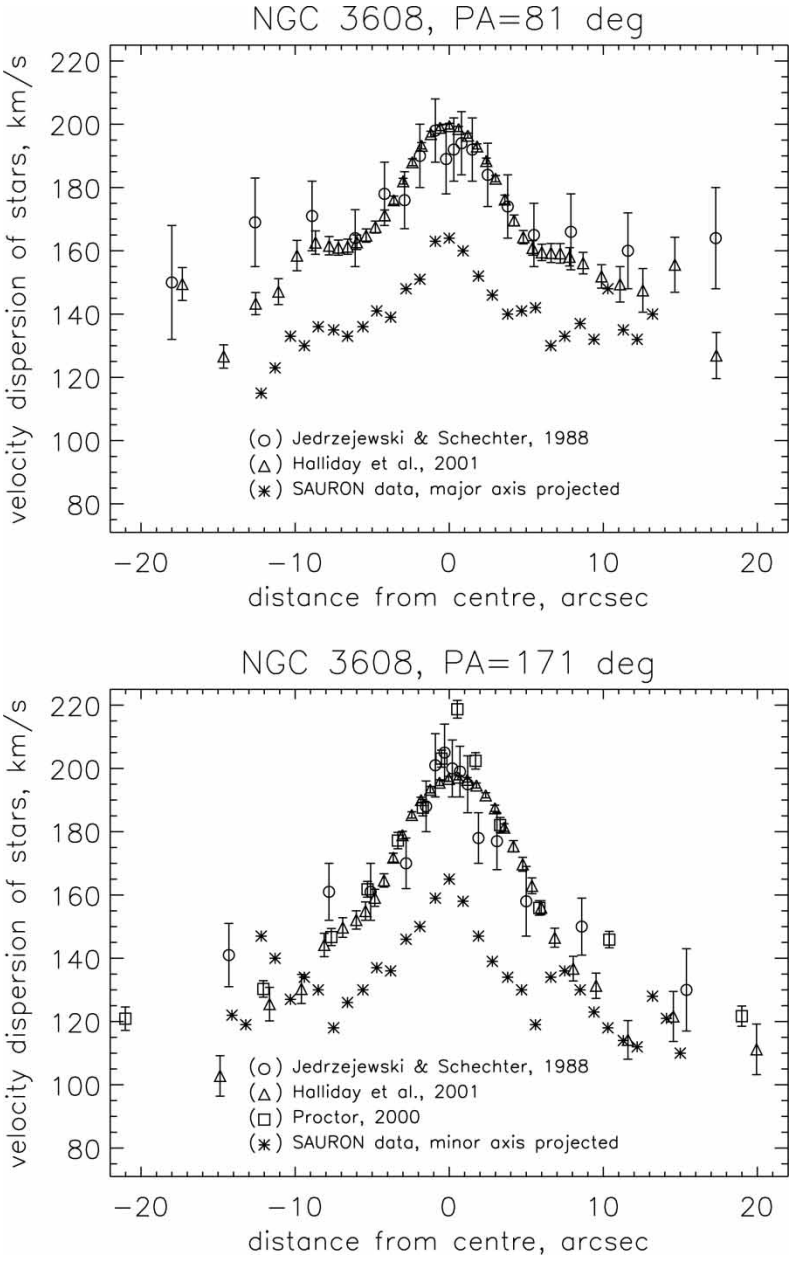

Figure 20. The comparison of the stellar velocity dispersion profiles simulated along the major and minor axes by using the SAURON 2D velocity dispersion field for the stars in the centre of NGC 3608 with the literature data of [13], [53], and [25]. The slit width used in the simulations is $2''$.

higher magnesium absorption-line strength, but do not differ from their outskirts as concerning Fe5270 ($\langle$Fe$\rangle$) or Hβ.

The most popular hypothesis of the kinematically decoupled core origin is a hypothesis of smaller elliptical satellite sinking ([54], [13], [55]): the smaller ellipticals have denser cores that can survive during accretion onto a giant galaxy. When in [34] it was found that the kinematically decoupled core of NGC 4365 is also magnesium-enhanced, the borders

of both decoupled rotation and magnesium enhancement being coincident, a hypothesis was suggested that the decoupled core of NGC 4365 was formed in a secondary star formation burst after a dissipative minor merger and subsequent gas accumulation in a circumnuclear disk. Bearing in mind that NGC 3607 and NGC 3608 resemble NGC 4365 as regards kinematically decoupled, magnesium-enhanced cores, for the former two galaxies we would, however, reject both hypotheses on the decoupled core origin mentioned above. The decoupled cores of NGC 3607 and NGC 3608 cannot be accreted small ellipticals because the galaxies have peaks of stellar velocity dispersion and of magnesium-line strength just in the centres of the decoupled cores, whereas in the frame of the dissipationless accretion scenario the satellite light must dominate in the centre of the merger product and so must demonstrate a lower metallicity in the centre than that of the giant hosts, and the velocity dispersion must have a dip [55]. But the scenario of [34] is also inapplicable: in the frame of the dissipative merger hypothesis, the formation of metal-enriched stars must proceed in a circumnuclear disk, and in the cases of NGC 3607 and NGC 3608 we have assured ourselves that the magnesium-enhanced structures are not disks. In both galaxies the areas of the maximum stellar velocity dispersion are elongated just as the magnesium-enhanced areas are; meantime dynamical simulations show that in a triaxial potential the high velocity dispersion areas have an oval shape and are aligned with the model bars [36]. The association of the magnesium-enhanced areas in NGC 3607 and NGC 3608 with some triaxial ellipsoidal structures is confirmed also by lack of disk-like rotation, if tracing the major axes of these structures. In NGC 3607 the magnesium-enhanced circumnuclear feature is elongated directly to the kinematical major axes of the stars and of the ionized gas – evidently, it is orthogonal to the circumnuclear disk major axis. In NGC 3608 the stellar rotation, though proceeding with the expected spin orientation, is very slow for the visible ellipticity of the magnesium-index isolines: if we attribute the Mgb-isoline ellipticity, 0.33, to a hypothetical circumnuclear disk, then the minimum v_{max}/σ ratio appropriate to oblate spheroids or disks would be 0.7 [56], and we have only $\sim$0.1 in the centre of the galaxy. After all, the ionized gas rotates in the polar plane. Both chemically decoupled cores in NGC 3607 and NGC 3608 look like small magnesium-enriched triaxial structures with some kinds of polar disks around them – only gaseous one in NGC 3608 and stellar-gaseous one in NGC 3607. We think that such a configuration may be possible if it occurs inside a global triaxial spheroid.

Though NGC 3607 is classified as S0, some investigators, e.g. [13], thought it to be an elliptical capturing its diffuse outer envelope from NGC 3608 during their interaction. Perhaps, there exists a principal difference between formation mechanisms for the decoupled cores in elliptical and disk galaxies. In disk galaxies the chemically decoupled structures are indeed circumnuclear stellar disks in the most cases. And when we have found such structures in the lenticular galaxies NGC 1023 [57] and NGC 3384 [1], we have noted that they are distinguished by a higher strength of both magnesium and iron absorption lines, the iron-index enhancement being slightly more extended than that of the Mgb. We then concluded that the secondary star formation bursts having produced the decoupled cores, were brief and effective in the unresolved nuclei, resulting in their increased [Mg/Fe], and prolonged during at least a few Gyr in the circumnuclear disks. In the centres of NGC 3607 and NGC 3608, which may accrete gas from a 3D quasi-spherical hot halo, and not from an outer fast-rotating disk nor from a supergiant flat gaseous ring as is the case of Leo I group, there were perhaps no initially favourable conditions for disk formation. With spheroidal geometry of the bursts, their duration is short, and only magnesium enhancement has time to be imprinted into the secondary stellar populations.

An interesting detail is the absence of age difference between the decoupled cores and the main bodies of NGC 3607 and NGC 3608. In disk galaxies, including the above mentioned lenticulars NGC 1023 and NGC 3384, the chemically decoupled cores are always ‘younger’

than the bulges, the mean (luminosity-averaged) stellar age of the nuclei being 3–7 Gyr versus 10–15 Gyr of the bulges. This implies that the secondary star formation bursts producing decoupled cores in the disk galaxies are rather recent. In NGC 3607 and NGC 3608 the decoupled cores do not seem to be distinguished by a younger mean age of the stellar population and, according to our estimates, are in any case older than 5 Gyr. Proctor [25] who studied radial profiles of the stellar population properties along the minor axes of NGC 3607 and NGC 3608 with the long-slit spectra has not found any age breaks at $R = 5'' - 6''$ too, though his Lick index calibration and so the absolute age estimates differ from ours. Finally, in [58] 2D distributions of the stellar population properties were studied in the centre of NGC 4365, the elliptical galaxy with kinematically decoupled core, and again any age difference between the core and its broad outskirts was not found, both being rather old, $T \geq 12$ Gyr. This age 'homogeneity' seems to be in some contradiction with the hypothesis of the secondary nuclear star formation burst having produced the decoupled cores. However, it can be explained by the older age of the decoupled cores in elliptical galaxies: as the photometric and spectral evolution becomes very slow at larger ages, one needs a very high precision of the measured Lick indices to detect age difference of a few Gyr when both decoupled cores and their outskirts are older than, say, 8 Gyr. When a larger statistics on the ages of decoupled cores in elliptical galaxies become available, this idea would be checked more carefully.

Acknowledgements

We thank Dr A. V. Moiseev of SAO RAS for supporting the observations at the 6 m telescope. The 6 m telescope is operated under the financial support of Science Ministry of Russia (registration number 01-43). During the data analysis we have used the Lyon-Meudon Extragalactic Database (LEDA) supplied by the LEDA team at the CRAL-Observatoire de Lyon (France) and the NASA/IPAC Extragalactic Database (NED) which is operated by the Jet Propulsion Laboratory, California Institute of Technology, under contract with the National Aeronautics and Space Administration. The research is partly based on the data taken from the ING Archive of the UK Astronomy Data Centre and on observations made with the NASA/ESA Hubble Space Telescope, obtained from the data archive at the Space Telescope Science Institute, which is operated by the Association of Universities for Research in Astronomy, Inc., under NASA contract NAS 5-26555. The study of the central evolution of the galaxies in groups was supported by a grant from the Russian Foundation for Basic Researches 04-02-16087 and the study of the evolution of galactic centres – by the Federal Scientific-Technical Program – contract of the Science Ministry of Russia no.40.022.1.1.1101.

References

[1] O.K. Sil'chenko, A.V. Moiseev, V.L. Afanasiev *et al.*, Astrophys. J. **591** 185 (2003).
[2] S.E. Schneider, Astrophys. J. **288** L33 (1985).
[3] S.E. Schneider, Astrophys. J. **343** 94 (1989).
[4] G. Giuricin, C. Marinoni, L. Ceriani and A. Pisani, Astrophys. J. **543** 178 (2000).
[5] A. Mahdavi and M. Geller, Astrophys. J. **554** L129 (2001).
[6] Y.Terashima, N. Iyomoto, L.C. Ho and A.F. Ptak, Astrophys. J. Suppl. Ser. **139** 1 (2002).
[7] P. Biermann, Ph.P. Kronberg and B.F. Madore, Astrophys. J. **256** L37 (1982).
[8] J.L. Tonry, A. Dressler, J.P. Blakeslee *et al.*, Astrophys. J. **546** 681 (2001).
[9] J.S. Mulchaey, D.S. Davis, R.F. Mushotzky and D. Burstein, Astrophys. J. Suppl. Ser. **145** 39 (2003).
[10] J.C. Shields, Astron. J. **102** 1314 (1991).
[11] F. Macchetto, M. Pastoriza, N. Caon *et al.*, Astron. Astrophys. Suppl. Ser. **120** 463 (1996).
[12] K.P. Singh, T.P. Prabhu, A.K. Kembhavi and P.N. Bhat, Astrophys. J. **424** 638 (1994).
[13] R. Jedrzejewski and P.L. Schechter, Astrophys. J. **330** L87 (1988).
[14] C.M. Carollo, M. Franx, G.D. Illingworth and D.A. Forbes, Astrophys. J. **481** 710 (1997).
[15] R. Bender, S. Döbereiner and C. Möllenhoff, Astron. Astrophys. Suppl. Ser. **74** 385 (1988).
[16] R. Bacon, G. Adam, A. Baranne *et al.*, Astron. Astrophys. Suppl. Ser. **113** 347 (1995).

[17] G. Worthey, S.M. Faber, J.J. González and D. Burstein, Astrophys. J. Suppl. Ser. **94** 687 (1994).
[18] V.L. Afanasiev, S.N. Dodonov and A.V. Moiseev, In: *Stellar dynamics: from classic to modern*/ Eds. Osipkov L.P. and Nikiforov I.I., Saint Petersburg Univ. press, 103 (2001).
[19] G. Worthey, Astrophys. J. Suppl. Ser. **95** 107 (1994).
[20] R. Bottema, Astron. Astrophys. **197** 105 (1988).
[21] R. Bacon, Y. Copin, G. Monnet *et al.*, Mon. Not. R. Astron. Soc. **326** 23 (2001).
[22] V.L. Afanasiev and O.K. Sil'chenko, Astron. J. **124** 706 (2002).
[23] V.V. Vlasyuk, Astrofiz. issled. (Izv. SAO RAS) **36** 107 (1993).
[24] O.K. Sil'chenko, Astron. Zh. **71** 706 (1994).
[25] R.N. Proctor, PhD Thesis (2002).
[26] S.C. Trager, G. Worthey, S.M. Faber *et al.*, Astrophys. J. Suppl. Ser. **116** 1 (1998).
[27] D. Fisher, M. Franx and G. Illingworth, Astrophys. J. **459** 110 (1996).
[28] D. Thomas, C. Maraston and R. Bender, Mon. Not. R. Astron. Soc. **339** 897 (2003).
[29] J.J. González, PhD Thesis (University of California, Santa Cruz, 1993).
[30] A.I. Terlevich and D.A. Forbes, Mon. Not. R. Astron. Soc. **330** 547 (2002).
[31] L.C. Ho, A.V. Filippenko and W.L.W. Sargent, Astrophys. J. Suppl. Ser. **112** 315 (1997).
[32] G. Stasinska and I. Sodre Jr., Astron. Astrophys. **374** 919 (2001).
[33] H. Kuntschner, J.R. Lucey, R.J. Smith *et al.*, Mon. Not. R. Astron. Soc. **323** 615 (2001).
[34] R. Bender and P.Surma, 1992, Astron. Astrophys. **258** 250 (1992).
[35] P.T. de Zeeuw, M. Bureau, E. Emsellem *et al.*, Mon. Not. R. Astron. Soc. **329** 513 (2002).
[36] P. Vauterin and H. Dejonghe, Mon. Not. R. Astron. Soc. **286** 812 (1997).
[37] G. Monnet, R. Bacon and E. Emsellem, 1992, Astron. Astrophys. **253** 366 (1992).
[38] A.V. Moiseev and V.V. Mustsevoy, Astron. Lett. **26** 565 (2000).
[39] J. Binney, Mon. Not. R. Astron. Soc. **212** 767 (1985).
[40] R. Bacon, Astron. Astrophys. **143** 84 (1985).
[41] D. Fisher, Astron. J. **113** 950 (1997).
[42] N. Caon, D. Macchetto and M. Pastoriza, Astrophys. J. Suppl. Ser. **127** 39 (2000).
[43] G.A. Welch and L.J. Sage, Astrophys. J. **584** 260 (2003).
[44] W.E. Baggett, S.M. Baggett and K.S.J. Anderson, Astron. J. **116** 1626 (1998).
[45] E. Emsellem, M. Cappellari, R.F. Peletier *et al.*, Mon. Not. R. Astron. Soc. **352** 721 (2004).
[46] A. Tomita, K. Aoki, M. Watanabe *et al.*, Astron. J. **120** 123 (2000).
[47] A.J. Barth, L.C. Ho and W.L.W. Sargent, Astron. J. **124** 2607 (2002).
[48] O.K. Sil'chenko, V.V. Vlasyuk and A.N. Burenkov, Astron. Astrophys. **326** 941 (1997).
[49] V.L. Afanasiev and O.K. Sil'chenko, Astron. J **117** 1725 (1999).
[50] O.K. Sil'chenko, Astron. J. **120** 741 (2000).
[51] V.L. Afanasiev and O.K. Sil'chenko, Astron. J. **119** 126 (2000).
[52] O.K. Sil'chenko, Astron. Lett. **28** 207 (2002).
[53] C.Halliday, R.L. Davies, H. Kuntschner *et al.*, Mon. Not. R. Astron. Soc. **326** 473 (2001).
[54] J. Kormendy, Astrophys. J. **287** 577 (1984).
[55] M. Balcells and P.J. Quinn, Astrophys. J. **361** 381 (1990).
[56] G. Illingworth, Astrophys. J. **218** L43 (1977).
[57] O.K. Sil'chenko, Astron. J. **117** 2725 (1999).
[58] R.L. Davies, H. Kuntschner, E. Emsellem *et al.*, Astrophys. J. **548** L33 (2001).